ADVANCED FUNCTIONAL MATERIALS
www.afm-journal.de

Materials Views
www.MaterialsViews.com

Hydrophobic Nanoreactor Soft-Templating: A Supramolecular Approach to Yolk@Shell Materials

*Amandine Guiet, Caren Göbel, Katharina Klingan, Michael Lublow, Tobias Reier, Ulla Vainio, Ralph Kraehnert, Helmut Schlaad, Peter Strasser, Ivelina Zaharieva, Holger Dau, Matthias Driess, Jörg Polte, and Anna Fischer**

Due to their unique morphology-related properties, yolk@shell materials are promising materials for catalysis, drug delivery, energy conversion, and storage. Despite their proven potential, large-scale applications are however limited due to demanding synthesis protocols. Overcoming these limitations, a simple soft-templated approach for the one-pot synthesis of yolk@shell nanocomposites and in particular of multicore metal nanoparticle@metal oxide nanostructures (M_{NP}@MO_x) is introduced. The approach here, as demonstrated for Au_{NP}@ITO_{TR} (ITO_{TR} standing for tin-rich ITO), relies on polystyrene-*block*-poly(4-vinylpyridine) (PS-*b*-P4VP) inverse micelles as two compartment nanoreactor templates. While the hydrophilic P4VP core incorporates the hydrophilic metal precursor, the hydrophobic PS corona takes up the hydrophobic metal oxide precursor. As a result, interfacial reactions between the precursors can take place, leading to the formation of yolk@shell structures in solution. Once calcined these micelles yield Au_{NP}@ITO_{TR} nanostructures, composed of multiple 6 nm sized Au NPs strongly anchored onto the inner surface of porous 35 nm sized ITO_{TR} hollow spheres. Although of multicore nature, only limited sintering of the metal nanoparticles is observed at high temperatures (700 °C). In addition, the as-synthesized yolk@shell structures exhibit high and stable activity toward CO electrooxidation, thus demonstrating the applicability of our approach for the design of functional yolk@shell nanocatalysts.

1. Introduction

In the last years, yolk@shell or "rattle-type" nanomaterials have received considerable attention due to their promising applications in the fields of heterogeneous catalysis,[1–4] electrocatalysis,[2,5,6] gas sensing,[7,8] battery development,[9,10] and drug delivery.[5,11] Yolk@shell materials are composed of single (or multiple) nanoscaled cores of a material A encapsulated inside a hollow nanosphere of a material B (A@void@B, in short A@B). Depending on the envisioned application, the surrounding hollow shell can be dense or porous (permeable) allowing control of the interactions between the core and the outer environment.

For many applications, it has been shown that yolk@shell nanocomposites feature enhanced properties as a result of their unique structure on the nanometer scale. In the field of heterogeneous catalysis for example, it has been demonstrated that supported metal nanoparticle (M_{NP}) catalysts with a yolk@shell structure are highly resistant against temperature and/or reaction induced M_{NP} sintering, thus preserving the catalysts activity. As such, a variety of yolk@shell nanocatalysts have been designed, including M_{NP}@carbon,[12–14] M_{NP}@silica,[2,15] Au_{NP}@TiO_2,[16] and Au_{NP}@ZrO_2,[17,18] all superior in terms of catalytic activity and stability when compared to their non-yolk@shell counterparts.

Despite their proven potential, the application of yolk@shell structures remains however limited due to challenging and

Dr. A. Guiet, Dr. C. Göbel, Dr. M. Lublow, T. Reier, Dr. R. Kraehnert, Prof. P. Strasser, Prof. M. Driess, Prof. A. Fischer
Chemistry Department
Technical University Berlin
Straße des 17. Juni 135, 10623 Berlin, Germany
E-mail: anna.fischer@ac.uni-freiburg.de
K. Klingan, Dr. I. Zaharieva, Prof. H. Dau
Physics Department
Free University Berlin
Arnimallee 14, 14195 Berlin, Germany
Dr. M. Lublow, Prof. A. Fischer
Institute of Inorganic and Analytical Chemistry
University Freiburg
Albertstrasse 21, 79104 Freiburg, Germany
Dr. U. Vainio
Institute of Materials Research
Helmholtz-Zentrum Geesthacht
Max-Planck-Straße 1, 21502 Geesthacht, Germany
Prof. H. Schlaad
Institute of Chemistry
University of Potsdam
Karl-Liebknecht-Straße 24-25, 14476 Potsdam, Germany
Dr. J. Polte
Humboldt University of Berlin
Brook-Taylor-Straße 2, 12489 Berlin, Germany

DOI: 10.1002/adfm.201502388

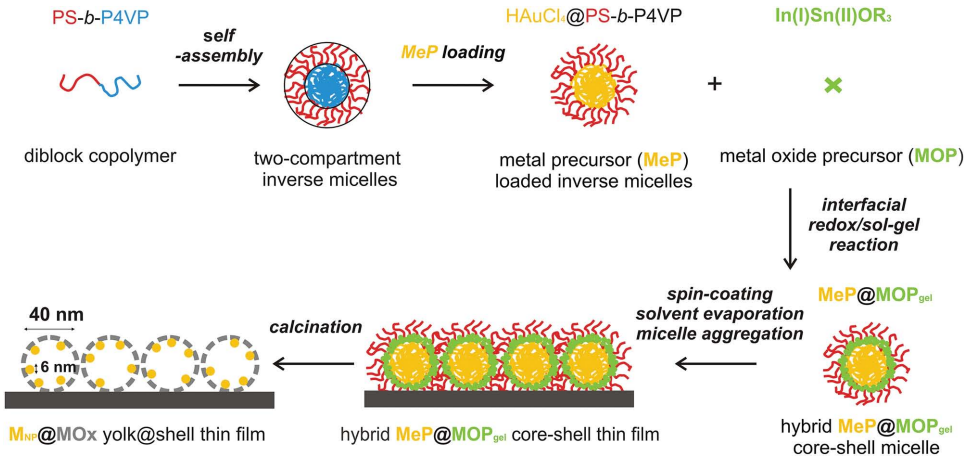

Scheme 1. Hydrophobic nanoreactor soft-templating—schematic representation of the four steps involved in the synthesis of $M_{NP}@ITO_{TR}$ nanostructures and in particular in the synthesis of $Au_{NP}@ITO_{TR}$ yolk@shell thin films.

fastidious synthesis protocols. Common routes imply multiple synthetic steps, involving colloidal synthesis of size controlled colloids, multicoating procedures with more or less expensive sacrificial template shells, as well as aggressive etching for template removal, all of these seriously impeding up-scaling and large-scale application.[19,20]

To overcome these limitations, we developed a simple and scalable approach allowing the one-pot synthesis of $M_{NP}@MO_x$ yolk@shell nanocomposites. As exemplified for gold and tin-rich ITO (ITO_{TR}),[21–24] the resulting $Au_{NP}@ITO_{TR}$ yolk@shell nanocomposites are composed of finely dispersed Au_{NP} (≈6 nm in diameter) strongly anchored onto the inner surface of porous ITO_{TR} hollow spheres (≈35 nm in diameter). As depicted in **Scheme 1** and demonstrated in the following, $M_{NP}@MO_x$ synthesis is achieved in four simple steps including: (1) Incorporation of a hydrophilic, acidic, and water containing metal precursor into the hydrophilic P4VP micellar core (e.g., $HAuCl_4 \cdot 3H_2O$ for $Au_{NP}@ITO_{TR}$), (2) incorporation of a hydrophobic alkoxidic metal oxide precursor into the hydrophobic PS micellar shell (e.g., indium(I)tin(II)tri-*tert*-butoxide (ITBO)[21–24] for $@ITO_{TR}$), (3) solution processing including solvent evaporation and micellar aggregation (e.g., dip-coating, spin-coating, or spraying), and (4) calcination at elevated temperature inducing concomitant polymer decomposition, metal oxide formation, and metal precursor reduction/nanoparticle formation.

As such, taking advantage of the compartmented structure of polystyrene-*block*-poly(4-vinylpyridine) (PS-*b*-P4VP) inverse micelles, our approach allows in a one-pot fashion simultaneous control over the composition and size of the metallic yolk components as well as of the size and composition of the metal oxide shell component (see Scheme 1).

2. Results and Discussion

As depicted in Scheme 1, $Au_{NP}@ITO_{TR}$ yolk@shell structures and in particular $Au_{NP}@ITO_{TR}$ yolk@shell-based thin films are synthesized by simply mixing three components in solution: PS-*b*-P4VP as template; $HAuCl_4 \cdot 3H_2O$ as hydrophilic, hydrated, and acidic gold precursor; and $[In(OtBu)_3Sn]$ as hydrophobic ITO_{TR} precursor.[21–24]

Following, the major processes involved in material synthesis as well as the major correlations between synthesis parameters and material structure are described. To begin micelles formation and selective core/corona incorporation of the gold and ITO_{TR} precursors are described in Sections 2.1 and 2.2, respectively. Following, the structure and nature of the resulting materials after solution processing and calcination are extensively investigated in Section 2.3. The driving force for yolk@shell formation is elucidated in Section 2.4, while influence of the gold precursor loading on the materials structure and composition is examined in Section 2.5. Insights into gold nanoparticle formation as well as particle accessibility are given in Sections 2.6 and 2.7, respectively. In Section 2.8, the applicability of the $Au_{NP}@ITO_{TR}$ yolk@shell structures for electrocatalytic applications is demonstrated by CO electrooxidation in alkaline media. Finally, the versatility of our approach is demonstrated in Section 2.9 with the direct synthesis of worm-like yolk@shell materials.

2.1. Micellar Structure and Metal Precursor Loading in PS-*b*-P4VP Inverse Micelles

The formation and structure of PS-*b*-P4VP inverse micelles in toluene as well as their $HAuCl_4$ loading capacity were studied by small angle X-ray scattering (SAXS) and anomalous small angle X-ray scattering (ASAXS). PS-*b*-P4VP inverse micelles, with a hydrophilic P4VP core and a hydrophobic PS shell, were formed by supramolecular self-assembly of PS_{111}-*b*-$P4VP_{96}$ unimers in toluene (**Table 1**). To determine the size and shape of the PS-*b*-P4VP micelles, SAXS measurements, sensitive to electron density variations at the nanometer scale, were performed. The recorded scattering curves depicted in **Figure 1** are typical for diluted solutions of noninteracting spherical objects. The curves could be fitted at best using a spherical core–shell scattering model (see Figures S1 and S2, Supporting Information, for details).[24] Accordingly data analysis revealed the formation of spherical inverse micelles (64 nm in diameter), composed of

Table 1. Number- and weight average molar masses (M_n and M_w), dispersity indexes M_w/M_n, and compositions (molar ratios S:4VP) of PS_{111}-*b*-$P4VP_{96}$ and PS_{135}-*b*-$P4VP_{137}$.

	M_n [kg mol^{-1}]	M_w [kg mol^{-1}]	M_w/M_n	Molar ratio S:4VP	Micelle morphology
PS_{111}-*b*-$P4VP_{96}$	21.7	27.5	1.27	1.14:1	Spherical
PS_{135}-*b*-$P4VP_{137}$	28.4	30.7	1.08	0.97:1	Worm-like

a P4VP electron-rich core (40 nm in diameter (R_{core} = 20 nm)) surrounded by a swollen PS corona (12 nm in thickness). It is important to mention that the size of the PS shell is likely underestimated in the SAXS analysis, as electron density gradients within the PS shell were not taken into account within the chosen core–shell model (Figure S3, Supporting Information).

Taking advantage of the metal cation affinity of the P4VP core,[24–28] the PS-*b*-P4VP polymer micelles could easily be loaded with variable amounts of $HAuCl_4 \cdot 3H_2O$. As evidenced by SAXS, 0.2, 0.3, and even 0.6 equivalents of $HAuCl_4 \cdot 3H_2O$ per pyridine unit could be loaded within the P4VP core affecting neither the micellar shape nor size (Figure 1). Indeed, as seen in Figure 1b, the shape of the scattering profile as well as the position of the curve minima remained unchanged with increasing $HAuCl_4 \cdot 3H_2O$ loading; clear indication that the shape and size of the micelles are largely unaffected by the gold precursor loading (Figures S4 and S5, Supporting Information). In contrast, the intensity of the scattering curve, which is proportional to the square of the scattering contrast, drastically increased with increasing gold loading (Figure 1b). Accordingly the electron density contrast between the micellar core and the surrounding solvent ($\Delta\eta_{core}$), which was determined by data fitting (see inset in Figure 1b), linearly increases with increasing gold loading; result which corroborates the homogenous and exclusive incorporation of the gold precursor within the hydrophilic P4VP core of the micelles.

The homogeneity of the $HAuCl_4 \cdot 3H_2O$ distribution inside the hydrophilic P4VP compartment was further confirmed by ASAXS (Figure 1c,d and Figures S6 and S7, Supporting Information). The ASAXS curves were recorded at three different energies in close vicinity of the Au L_3 absorption edge (^{79}Au L_3, E_{Au} = 11 919 eV, E_1 = 11 527 eV, E_2 = 11 873 eV, and E_3 = 11 915 eV). While the scattering contribution of the gold atoms within the P4VP core of the micelles is expected to vary

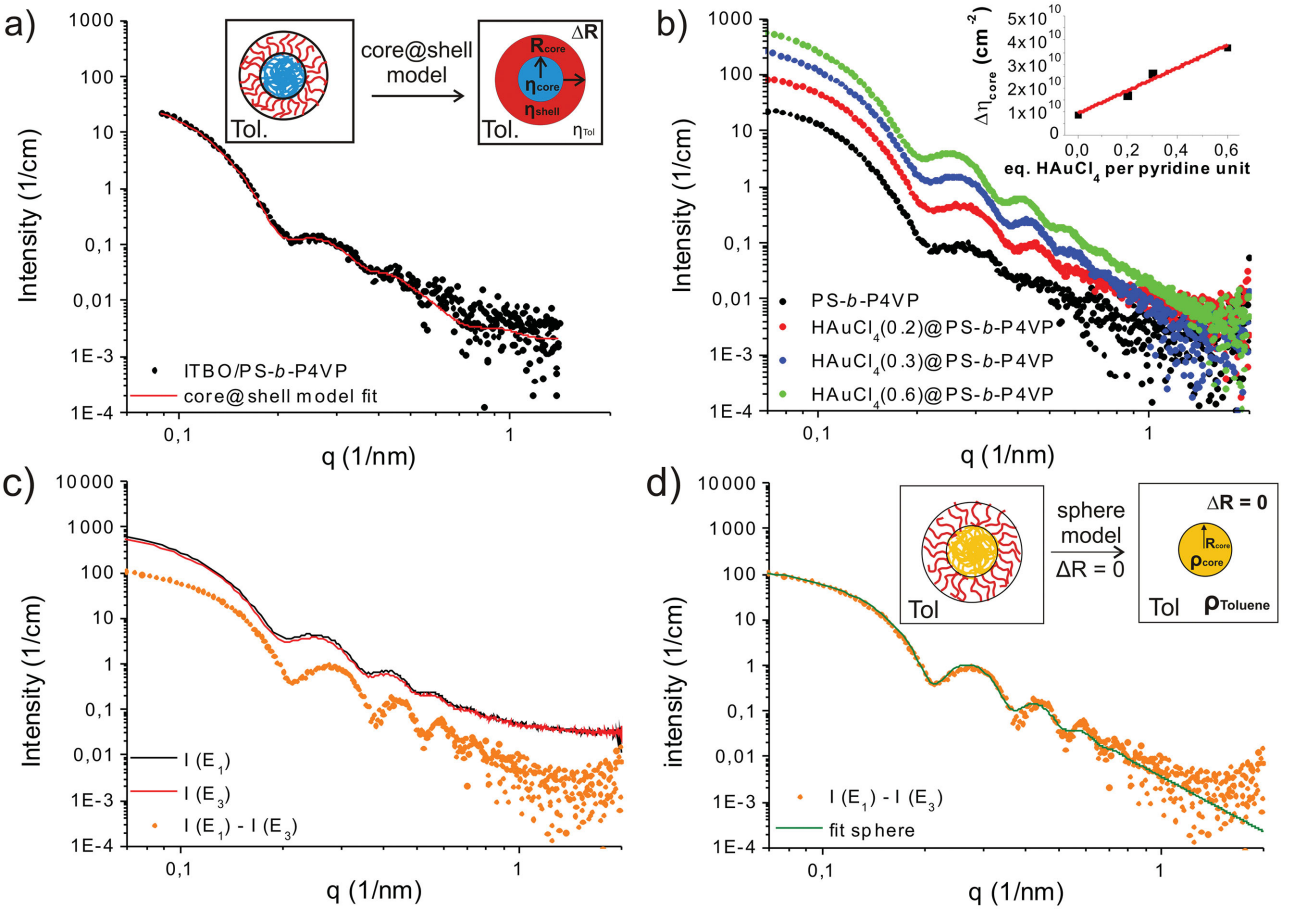

Figure 1. a) SAXS curve and corresponding fit (core–shell model) of PS-*b*-P4VP inverse micelles. b) SAXS scattering curves of unloaded (black) and $HAuCl_4$(*X*)@PS-*b*-P4VP loaded micelles with *X* = 0.2 (red), 0.3 (blue), and 0.6 (green) eq. of $HAuCl_4 \cdot 3H_2O$ per pyridine unit. Inset: Linear dependence of $\Delta\eta_{core}$ (scattering length density difference between the core and the solvent) with increasing $HAuCl_4 \cdot 3H_2O$ loadings. c) ASAXS curves recorded at E_1 = 11 525 eV (black curve) and E_3 = 11 915 eV (red curve) and resulting curve of their subtraction (orange curve). d) Fit of the subtracted ASAXS curve applying a sphere model (details in the Supporting Information).

close to the gold absorption edge, the scattering contribution of the polymer backbone should remain unchanged at energies far from the carbon absorption edge (^{6}C K-edge ≈290 eV). In a good approximation, the subtraction of the scattering curves measured at E_1 = 11 527 eV and E_3 = 11 915 eV yields the scattering contribution majorly related to the gold loaded domains (Figure 1c). As can be seen in Figure 1d, the gold contribution can be fitted with a spherical scattering model revealing a gold loaded spherical domain with a size corresponding approximately to the size of the micellar core. As such ASAXS confirms the homogeneous distribution of the gold precursor throughout the P4VP micellar core (Figure 1d and Figure S7, Supporting Information).

To summarize, SAXS and ASAXS reveal the formation of spherical PS-*b*-P4VP inverse micelles with a PS shell and a P4VP core, the latter exhibiting an excellent metal loading capacity, making PS-*b*-P4VP inverse micelles highly attractive templates for the synthesis of M_{NP}@support yolk@shell nanostructures.

2.2. Formation of Metal Precursor@Metal Oxide Hybrid Micelles in Solution

For the synthesis of Au_{NP}@ITO_{TR} yolk@shell materials selected amounts of ITBO were added to the previously described $HAuCl_4 \cdot 3H_2O$ loaded micellar solutions ($HAuCl_4$(*X*)@PS-*b*-P4VP with *X* = 0.2, 0.3, and 0.6 eq. of $HAuCl_4 \cdot 3H_2O$ per pyridine unit, Figure S8, Supporting Information). The yellow solutions turned immediately brown after the ITBO addition and in particular for higher gold loadings, indication for an immediate and stoichiometric reaction between the metal and the metal oxide precursor within the micelles. In line with these observations minor to major structural changes of the micelles were revealed by SAXS. As seen in **Figure 2**a, ITBO addition induces only minor changes in the SAXS curve in case of low $HAuCl_4 \cdot 3H_2O$ loadings (*X* = 0.2 eq.); result which indicates a homogeneous distribution of the ITBO precursor within the PS shell and the solvent toluene.[24] In contrast, for higher loadings (*X* = 0.3 and *X* = 0.6) a large increase of the scattering intensity as well as a shift to lower *q* values of the form factor minima is observed (Figure 2b,c). These drastic changes can be explained either by the formation of larger micelles or—as depicted in Scheme 1—by the formation of core@shell@shell structures exhibiting a newly formed electron density rich shell at the P4VP/PS interface. Considering the respective polarity of the metal and metal oxide precursors (i.e. $HAuCl_4 \cdot 3H_2O$ and ITBO), their initial repartition in the inverse micelle as well as their reactivity (ITBO is highly sensitive toward oxidation, hydrolysis, and condensation), the formation of core@shell@shell structures, as a result of an interfacial inter-precursor reaction at the P4VP/PS interface, seems more than likely.

Neglecting in a first approximation the scattering contribution of the swollen PS shell, the SAXS data could best be fitted employing a core–shell model composed of a ≈40 nm in diameter electron density rich core surrounded by a ≈1.7 nm thick electron density rich shell (Figure S9, Supporting Information). As such, strong indication for the formation of an ITBO derived shell via hydrolysis–condensation at the P4VP/PS core/corona interface is given in the presence of higher $HAuCl_4 \cdot 3H_2O$ loadings. Further spectroscopic corroboration of this hypothesis will be given in Section 2.4.

To summarize, SAXS analysis revealed that depending on the precursor's stoichiometry different types/structures of metal precursor@metal oxide micelles are formed in solution comprising a more or less developed ITBO derived shell at the PS/P4VP interface.

2.3. Nanostructured Au_{NP}/ITO_{TR} Thin Films: Relation between Micellar Structure and Material Structure

For the synthesis of Au_{NP}@ITO_{TR} yolk@shell thin films, the previously described $HAuCl_4$@ITBO precursor micelles were spin-coated onto selected substrates (among others silicon). The resulting hybrid films were dried and subsequently calcined at 400 °C for 2 h in air to induce ITO_{TR} formation, polymer decomposition, and gold nanoparticle formation. Investigation of the formed nanostructures was performed with scanning electron microscopy (SEM) (Figure 2). In line with the previously described SAXS results, SEM measurements revealed the formation of different types of Au_{NP}/ITO_{TR} nanostructures for different $HAuCl_4 \cdot 3H_2O$ loadings (i.e., different $n(HAuCl_4 \cdot 3H_2O)/n(ITBO)$ molar ratios, Figure S8, Supporting Information). As such, low $HAuCl_4 \cdot 3H_2O$ loadings (i.e., low $n(HAuCl_4 \cdot 3H_2O)/n(ITBO)$ ratios) lead to mesoporous ITO_{TR} thin films with an open porous structure, homogeneously loaded with one size-controlled Au_{NP} per pore of ≈6 nm in diameter (SEM images, Figure 2d).[24] In contrast, higher $HAuCl_4 \cdot 3H_2O$ loadings (i.e., higher $n(HAuCl_4 \cdot 3H_2O)/n(ITBO)$ ratios) resulted in thin films build of closely packed yolk@shell nanostructures (see Figure 2e,f). As revealed by scanning electron microscopy (SEM, Figure 2), transmission electron microscopy (TEM) (**Figure 3**), energy dispersive X-ray spectroscopy (EDX) (Figure S11, Supporting Information), X-ray diffraction (XRD) (Figure 3), and X-ray photoelectron spectroscopy (XPS) (Figure S12, Supporting Information), these structures are composed of ≈40 nm (in diameter) ITO_{TR} hollow spheres with a shell thickness of ≈2.5 nm (Figure S13, Supporting Information), all filled with multiple, finely dispersed, and uniformly sized ≈6 nm Au_{NP} per sphere (Figures 2e,f and 3).

The formation of Au^0 was thereby evidenced by XRD, high resolution TEM (HRTEM), and XPS. The X-ray diffraction pattern of the samples calcined at 400 °C featured broad Au^0 reflections in line with the JCPDS file No. 04-0784 for Au^0 (space group Fm3m). In addition, HRTEM measurements performed on the nanoparticles anchored on the inner side of the shell, revealed lattice fringes in line with the $d_{(111)}$ lattice distance of Au^0. Finally, XPS also revealed the presence of Au^0 in the nanocomposites (Figure S12, Supporting Information). On the other hand, formation of amorphous ITO_{TR} with an In to Sn ratio close to 1 was revealed by XRD, EDX, and XPS.[21,23,29] No contribution of crystalline tin doped indium oxide (ITO, Sn:In_2O_3), indium oxide (In_2O_3), or tin oxide (SnO_2) could be observed in the XRD pattern, while Sn, In, and O were detected by EDX in a ratio of ≈1:1:2 (see Figure S11, Supporting Information) with

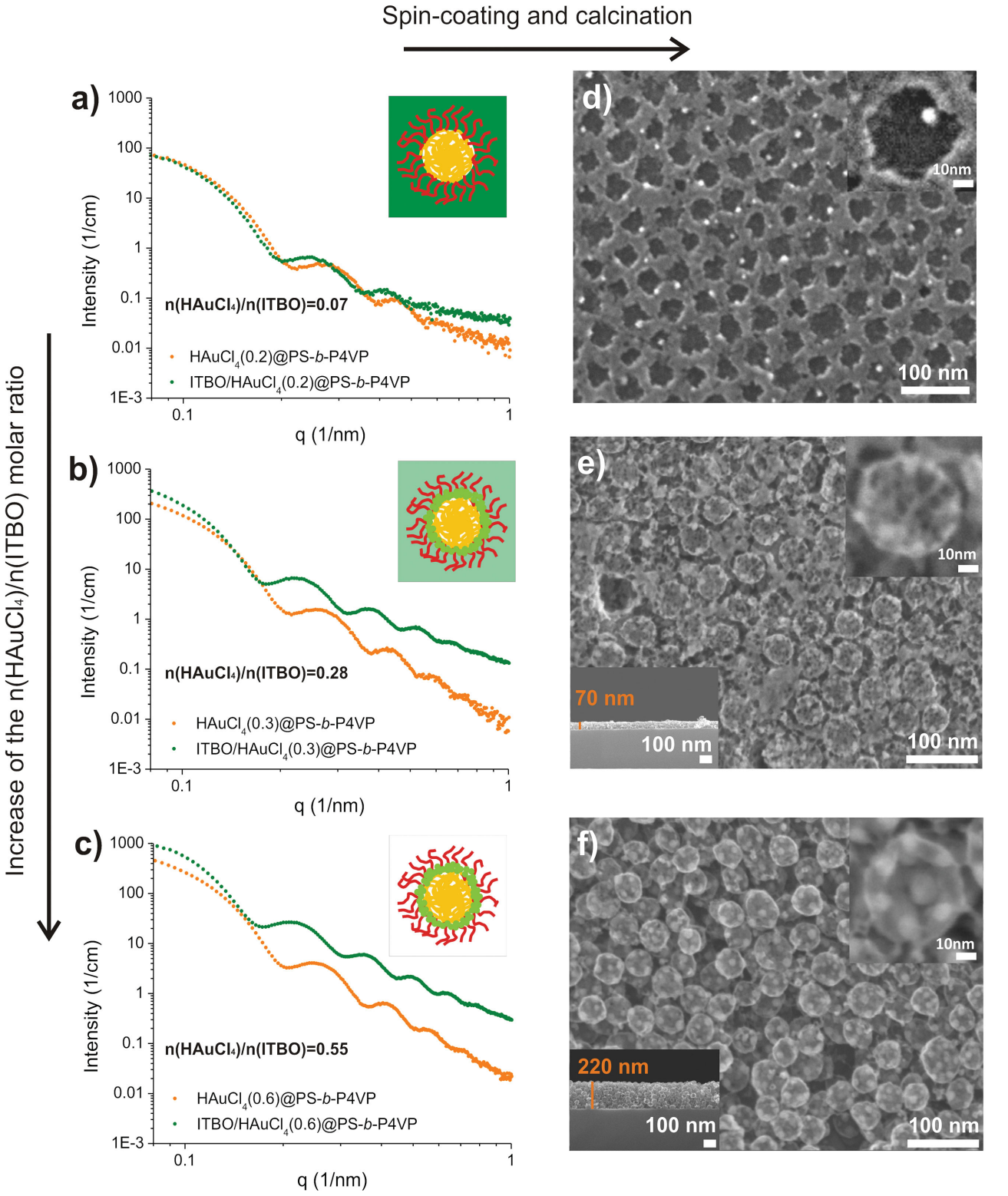

Figure 2. SAXS scattering curves of $HAuCl_4 \cdot 3H_2O$ loaded inverse micelles before (orange curves) and after (green curves) the addition of ITBO with *n*Au/*n*ITBO of a) 0.07,* b) 0.28, and c) 0.55. Top-view and cross-sectional SEM images of thin films after spin-coating the previous micellar solutions on Si wafers followed by calcination in air at 400 °C (*n*Au/*n*ITBO = d) 0.07,* e) 0.28, and f) 0.55). *Adapted with permission.[24] Copyright 2014, American Chemical Society.

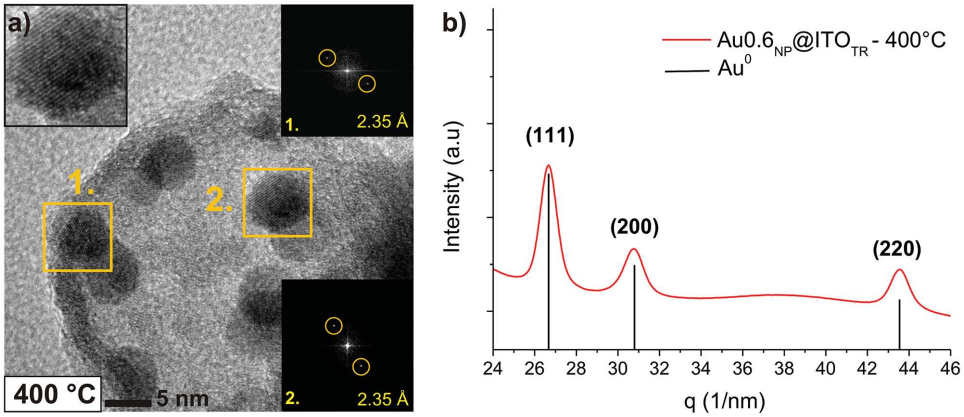

Figure 3. a) HRTEM image of one single $Au0.6_{NP}@ITO_{TR}$ yolk@shell particle scratched from a thin film calcined at 400 °C. The insets represent the FFTs of the marked areas. A lattice spacing of 2.35 Å could be determined corresponding to the lattice distance $d_{(111)}$ of crystalline gold. b) XRD pattern of $Au0.6_{NP}@ITO_{TR}$ calcined at 400 °C thin films deposited on ultra thin Si [100] (transmission measurement).

In and Sn present in the oxidation state +III and +IV, respectively (Figure S12, Supporting Information).[24]

From all these results we could conclude that the structure and composition of the Au_{NP}/ITO_{TR} nanocomposites are imprinted by the structure and composition of the $HAuCl_4$@ITBO precursor micelles (see previous SAXS results). In case no shell formation occurs within the micelles (i.e., for low $HAuCl_4$ loadings), mesostructured ITO_{TR} thin films with an open porous structure and a gold loading of one Au_{NP} (≈6 nm) per pore are obtained. In contrast, in case shell formation occurs within the micelles (i.e., for high $HAuCl_4$ loadings), Au_{NP}/ITO_{TR} nanocomposites with a yolk@shell nanostructure, composed of multiple Au_{NP} (≈6 nm) encapsulated inside 40 nm ITO_{TR} hollow spheres, are obtained. In addition, increasing the gold precursor loading does not only lead to the observed nanostructural transformation but also affects the porosity of the ITO_{TR} shells (see SEM data in Figure 3).

Important to note is that independent of the gold precursor loading, the size of the Au_{NP} is always centered around 6 nm (for samples calcined at 400 °C). As such 6 nm seems to be an energetically stable size for Au_{NP} grown on an ITO_{TR} interface heated to 400 °C (see Figure 5). This result suggests a strong Au–ITO_{TR} metal–support interaction allowing the stabilization of the particle dispersion on the amorphous ITO_{TR} support. Considering that the particle formation occurs on a highly amorphous metal oxide surface, a high density of —OH surface functionalities can be assumed which might help to stabilize the forming nanoparticles.

2.4. Interfacial Reactivity as Driving Force for Yolk@Shell Formation

To reveal the driving force responsible for the ITBO derived shell formation, X-ray absorption spectroscopy (XAS) and ^{119}Sn-nuclear magnetic resonance (NMR) measurements were performed. For this purpose, three different solutions containing ITBO, ITBO in the presence of unloaded PS-*b*-P4VP micelles (ITBO/PS-*b*-P4VP), and ITBO in the presence of $HAuCl_4 \cdot 3H_2O$ loaded PS-*b*-P4VP micelles (ITBO/$HAuCl_4$(*X*)@PS-*b*-P4VP) were investigated. Information about the average oxidation states of In and Sn in the different precursor solutions were gained by XAS at the L-edges of the metals, as the shape and position of an element specific absorption edge depends on the element oxidation state and local environment (^{49}In L_3 = 3730 eV and ^{50}Sn L_2 = 4156 eV). As can be seen for the indium and tin edge in **Figure 4** a,1 and Figure S14,1 (Supporting Information), no difference is observed between the XAS spectra of ITBO and ITBO in the presence of PS_{111}-*b*-$P4VP_{96}$ micelles. This suggests that Sn and In maintain their initial oxidation states (i.e., Sn(II) and In(I)) and remain in their initial coordination. In contrast, when ITBO is added to $HAuCl_4 \cdot 3H_2O$ loaded PS-*b*-P4VP micelles, clear evidence for an increasing oxidation state with increasing $HAuCl_4 \cdot 3H_2O$ loading is observed at the indium edge (Figure 4a). For the highest gold loading of 0.6 equivalents, the position of the In edge is even similar to the one recorded for an In(III)(O*t*Bu)$_3$ reference, evidencing the quantitative oxidation of the In(I) to In (III) in the presence of $HAuCl_4 \cdot 3H_2O$. In contrast, no such change is observed in the position of the Sn edge (Figures S14,2 and 3, Supporting Information), which suggests that Sn remains as Sn(II). However, closer examination of the XAS spectra at the Sn edge reveals a change in the first coordination sphere of tin (see comparison between the XAS spectra of ITBO and Sn(II)(OtBu)$_2$, marked oscillations in Figure S14,2 and 3, Supporting Information); change which might result from a ligand substitution/addition at the tin center. In line with the XAS results, room-temperature ^{119}Sn-NMR confirms that a reaction between the ITBO and the $HAuCl_4 \cdot 3H_2O$ precursors takes place within the micelles. While no change of the ^{119}Sn-NMR spectra of ITBO is observed in the presence of unloaded polymer micelles, two new Sn(II) species (δ = −148 ppm and δ = −170 ppm) are formed in case of $HAuCl_4 \cdot 3H_2O$ loaded micelles ($HAuCl_4$(*X*)@PS-*b*-P4VP). At intermediate loadings (*X* = 0.3), ITBO is only partially converted, as evidenced by the remaining ITBO signal at δ = −78 ppm (Figure 4b). In contrast, complete ITBO conversion is achieved at higher loadings (*X* = 0.6) in line with the complete disappearance of the ITBO signal at δ = −78 ppm (Figure 4b). Although it is not possible to determine the exact nature of the Sn(II) species, the formation of a two to three times coordinated Sn(II)–alkoxo–chloro species is very likely, as chemical shifts between −140 and −170 ppm are typical for these kind of Sn(II) compounds.[30,31]

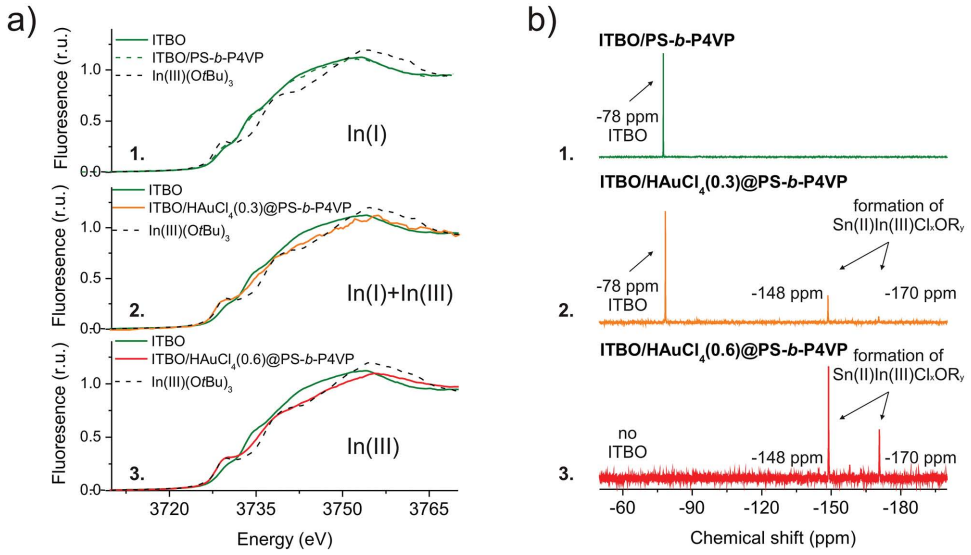

Figure 4. a) Indium L_3-edge XANES spectra of ITBO dissolved in toluene (green) compared with ITBO/PS-*b*-P4VP (1: dashed green), ITBO/$HAuCl_4$(0.3)@PS-*b*-P4VP (2: orange), ITBO/$HAuCl_4$(0.6)@PS-*b*-P4VP (3: red), and In(III)$(OtBu)_3$ (1, 2, 3: dashed black). b) ^{119}Sn-NMR spectra of ITBO/PS-*b*-P4VP (1: green), ITBO/$HAuCl_4$(0.3)@PS-*b*-P4VP (2: orange), and $HAuCl_4$(0.6)@PS-*b*-P4VP (3: red) in toluene-d_8.

As such XAS, NMR, and SAXS confirm an interfacial reaction between the gold precursor and the ITBO precursor, leading to a gold induced oxidation of In(I) to In(III) as well as to a ligand addition/substitution at the Sn(II) center. Considering the standard electrode potential of the following redox reactions the oxidation of In(I) to In(III) along with the concomitant reduction of the Au(III) atoms is indeed very likely

$$AuCl_4^- + 2e^- \rightarrow AuCl_2^- + 2Cl^- \left(E^0 = 0.92\,V\right) \quad (1)$$

$$In^+ \rightarrow In^{3+} + 2e^- \left(E^0 = -0.43\,V\right) \quad (2)$$

In addition, in view of the hydrate/acidic nature of the $HAuCl_4 \cdot 3H_2O$ precursor, hydrolysis–condensation of the highly reactive ITBO precursor is more than likely to take place at the P4VP/PS interface, thus leading to an ITBO derived shell formation within the micelles.

2.5. AuNP@ITO_{TR} Yolk@Shell Thin Films: Processability and Influence of the Gold Precursor Loading

As the structure-directing precursor micelles are formed in solution, our approach should in principle be compatible with all processing methods involving solvent evaporation. This includes, for example, spraying,[32] printing,[33] dip- or spin-coating,[24] as well as impregnation and so on. Despite their a priori hydrophobic nature, the solutions were easily coated on various substrates by either spin- or dip-coating. Interestingly, the viscosity of the ITBO/$HAuCl_4$(*X*)@PS-*b*-P4VP solutions increased with increasing $HAuCl_4 \cdot 3H_2O$ loading; observation in line with the hydrolysis–condensation hypothesis made earlier. As a result, the film thickness increased from 70 to 200 nm for an increasing gold loading of 0.3 and 0.6, respectively (Figure 2e,f). Further control of the film thickness could also be achieved by varying the concentration of the precursor solution, as illustrated for $Au0.6_{NP}$@ITO_{TR} thin films (Figure S15, Supporting Information). Bilayers of 50 nm as well as thick multilayers of 200 nm could thus be synthesized starting from diluted and concentrated precursor solutions, respectively ([PS-*b*-P4VP] = 10 mg L^{-1} and [PS-*b*-P4VP] = 30 mg L^{-1}, Figure S15, Supporting Information, and Experimental Section for experimental details). In all cases, the ITO_{TR} hollow spheres exhibit a diameter of 40 nm, in line with the size of the P4VP core domain of the precursor micelles (**Figure 5**). The limited thickness of the ITO_{TR} shell (2.5 nm) most probably results from the limited diffusion of the reacting precursors at the PS/P4VP interface. For all gold loadings, Au_{NP} of 6 nm in diameter are formed after calcination at 400 °C, demonstrating the existence of a stable Au_{NP} size for particles supported/grown on ITO_{TR} at 400 °C. This result is surprising considering that the Au_{NP} are formed in a very small volume and are separated by only a few nanometers and should thus be prone to sinter, especially at elevated temperatures (**Figure 6**).

As a result, increasing the $HAuCl_4 \cdot 3H_2O$ does not lead to an increase of the particle size, as would be expected in case of particle sintering, but rather increases the number of Au_{NP} encapsulated per hollow sphere. As such, ultrahigh particle loadings of ≈6–12 size controlled gold nanoparticles per hollow sphere could be obtained for $Au0.3_{NP}$@ITO_{TR} and $Au0.6_{NP}$@ITO_{TR}, respectively (Figure 5c,f).

2.6. Particle Formation and Growth

To generate further insight into the gold nanoparticle formation, we monitored their growth during calcination by ex situ TEM analysis (see data for $Au_{0.6NP}$@ITO_{TR} (Figure 6)). For that purpose, a monolayer of hybrid core–shell precursor micelles was deposited onto a temperature-resistant silicon nitride membrane TEM grid and calcined to different temperatures. The grid was measured

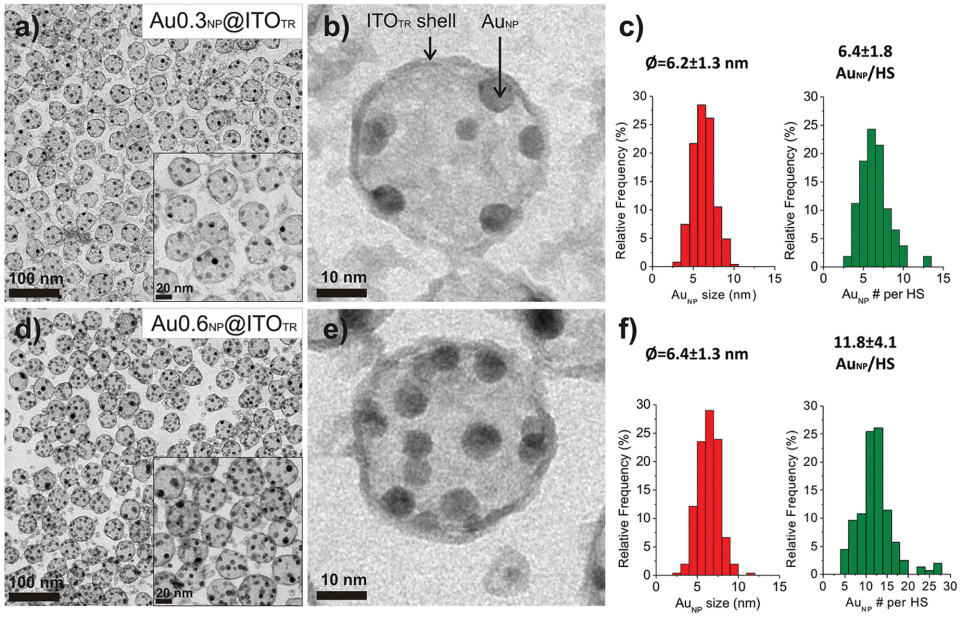

Figure 5. TEM images at low and high magnification of a,b) $Au0.3_{NP}@ITO_{TR}$ and d,e) $Au0.6_{NP}@ITO_{TR}$ monolayers deposited on SiN TEM grids after calcination at 400 °C for 2 h. c,f) Corresponding size distribution of Au_{NP} and number of NPs per hollow spheres (HS).

directly after film deposition (using a special TEM holder providing N_2 atmosphere prior column insertion) and at different stages of the calcination (i.e., between 200 and 700 °C). For the as-deposited micellar monolayer, TEM images revealed the formation of tiny Au_{NP} clusters (smaller than 2 nm in diameter) inside the P4VP core. As no evidence was given for Au_{NP} formation in solution, be it by UV–visible (UV–vis) spectroscopy or by SAXS (Figure S16, Supporting Information), we attribute these cluster formation to electron beam induced gold reduction. After calcination at 200 °C, multiple small Au_{NP} with a mean diameter of 3.6 ± 0.7 nm were formed. Further calcination at 300 °C leads to particle growth (from <2 to 4.8 ± 1.5 nm) along with a decrease of the particle number encapsulated per hollow sphere. The decomposition and reduction of the gold precursor at the origin of the particle formation could further be revealed by EDX (Figure S17, Supporting Information). As can be seen in the EDX spectra in Figure S17

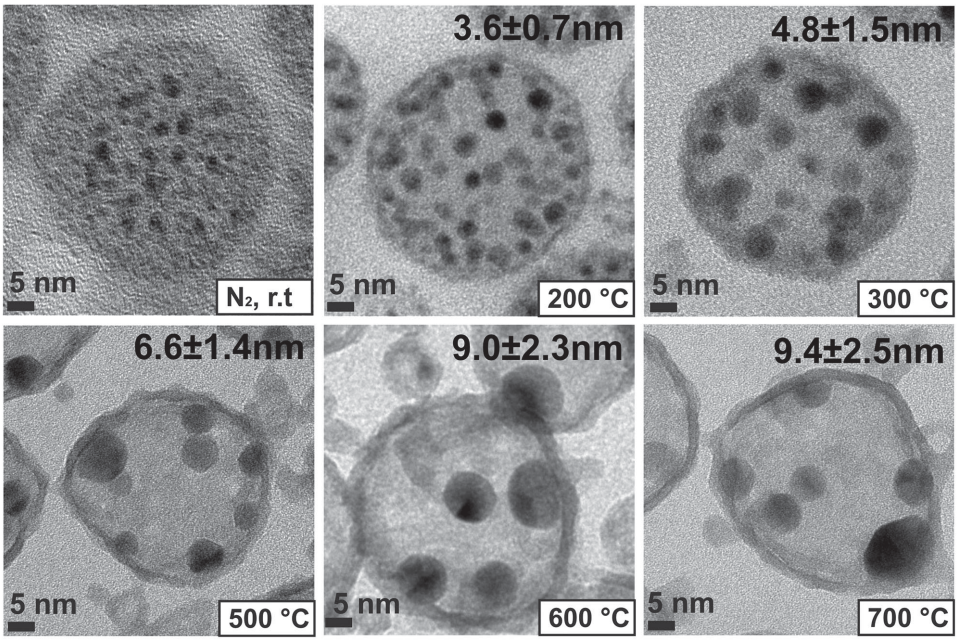

Figure 6. TEM images of $Au0.6_{NP}@ITO_{TR}$ yolk@shell nanostructures deposited on SiN membrane grids before calcination, i.e., under N_2, and calcined under air at 200 °C for 5 min and 300 °C for 5 min, 500 °C, 600 °C, and 700 °C for 2 h.

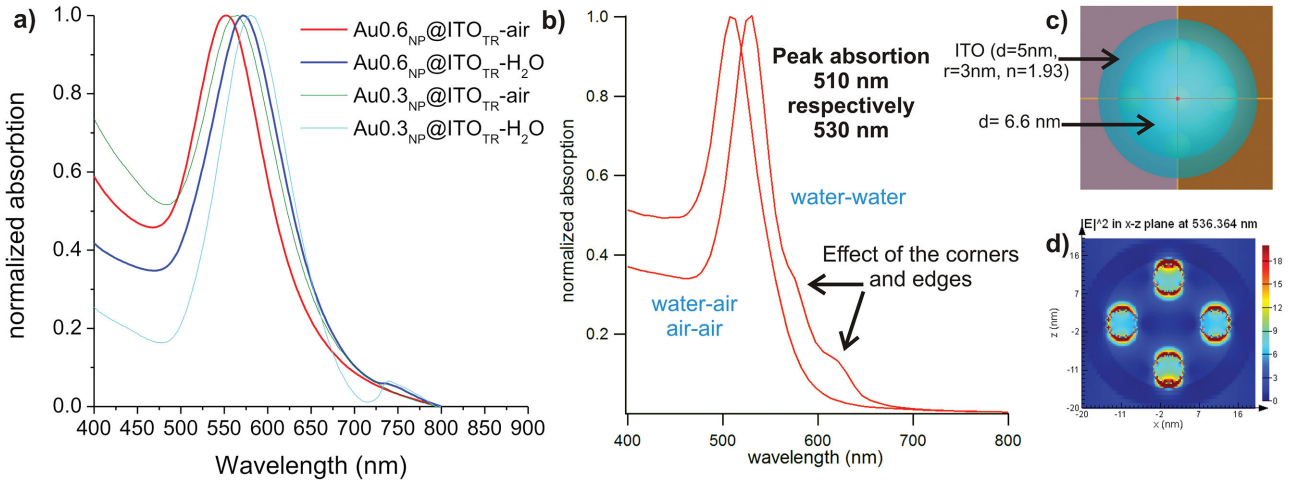

Figure 7. a) UV–vis spectroscopy measurements of $Au0.3_{NP}@ITO_{TR}$ and $Au0.6_{NP}@ITO_{TR}$ yolk@shell based films deposited on glass substrate before and after immersion in H_2O respectively. b) Calculated wavelength shift expected for an $Au_{NP}@ITO$ model hollow sphere (see drawing in the inset) immersed in air (air–air) and immersed in water with no water inside the sphere (water–air) and with water inside the sphere (water–water). The air–air and water–air curves are identical and thus overlay.

(Supporting Information), the Cl signal progressively decreases with increasing temperature until it completely vanishes at 400 °C; results which are in line with the thermal gravimetric analysis (TGA) results of the gold precursor decomposition (Figure S18, Supporting Information). Very interesting is the thermal stability of the gold nanoparticles at temperatures higher than 400 °C (Figure 6).

Indeed, despite a slight increase of the NPs size with increasing temperature (i.e., from 6.4 ± 1.3 nm at 400 °C to 9.4 ± 2.5 nm at 700 °C), the strong anchorage of the Au_{NP} onto the ITO_{TR} support seems to prevent complete sintering of the Au_{NP} into one particle per shell. As such, the particles stay remarkably small and homogeneously sized (<10 nm) up to 700 °C, even though they are separated by only a few nanometers. By inspection of the contact zone between the particles and the ITO_{TR} shell, one can see for some particles a curvature match between the particles and the oxide shell, which results in shoal cavities providing anchor points/surfaces for particle surface stabilization. In this context, the morphological stability of the ITO_{TR} hollow spheres up to 700 °C is certainly helpful for particle stabilization. Indeed, although crystallization of the amorphous matrix into In_2O_3 and SnO_2 occurs at temperature between 600 and 700 °C, the overall shape of the ITO_{TR} shell is fully preserved (Figures S19 and S20, Supporting Information).

2.7. AuNP@ITO_{TR} Yolk@Shell Thin Films: Shell Porosity and Particle Accessibility

In order to gain a better insight into the porosity of the $Au_{NP}@ITO_{TR}$ yolk@shell structures, Kr physisorption was performed. Considering the film thicknesses of 70 nm for $Au0.3_{NP}@ITO_{TR}$ and 220 nm for $Au0.6_{NP}@ITO_{TR}$, specific surface areas of 350 and 120 $m^2\ cm^{-3}$ were determined for $Au0.3_{NP}@ITO_{TR}$ and $Au0.6_{NP}@ITO_{TR}$, respectively. The higher value obtained for the $Au0.3_{NP}@ITO_{TR}$ yolk@shell thin film is in good agreement with the higher shell porosity observed for the $Au0.3_{NP}@ITO_{TR}$ yolk@shell particles by HRSEM (Figure 2e). Further elucidation of the particles accessibility was performed by exploiting their plasmonic properties, and in particular the dielectric constant dependent position of the localized surface plasmon resonance absorption band (LSPR). Indeed, according to Mie's theory,[34] any increase of the dielectric constant of the medium surrounding the Au_{NP} induces an LSPR shift toward lower energies (i.e., to higher wavelengths).[34,35] Thus, probing the LSPR position of the $Au_{NP}@ITO_{TR}$ films when immersed in air or in water allows evaluation of the particles' accessibility inside the hollow spheres. For both $Au0.3_{NP}@ITO_{TR}$ and $Au0.6_{NP}@ITO_{TR}$ samples, an LSPR absorption is observed by UV–vis spectroscopy (**Figure 7**a). In agreement with the gold nanoparticle size and the gold nanoparticle spacing, the position of the LSPR is very similar for both samples and comprised between 530 and 540 nm. In both cases, a redshift (with a similar magnitude of $\Delta\lambda \approx 20$ nm) is observed upon the transfer from air to water. A shift of similar magnitude ($\Delta\lambda \approx 20$ nm) was calculated for model ITO hollow spheres filled with 6.5 nm sized Au nanoparticles between an air–air or water–air configuration and a water–water configuration (see Figure 7b). As such this shift unambiguously demonstrates the penetration of water inside the hollow spheres and thus the accessibility of the Au_{NP} through the ITO_{TR} shell.

In view of the latter result, we could demonstrate that hydrophobic nanoreactor templating allows the synthesis of yolk@shell nanocomposites with fully accessible core particles, making these yolk@shell structures highly interesting for catalytic or sensing applications.

2.8. AuNP@ITO_{TR} Yolk@Shell Thin Films: Applicability as Electrodes for Electrocatalytic Applications

Considering the conductive nature of the $Au_{NP}@ITO_{TR}$ yolk@shell nanocomposites (σ = 11.4 S cm^{-1}, see Figure S10, Supporting Information), we evaluated their applicability as electrodes for electrocatalytic applications, in particular for

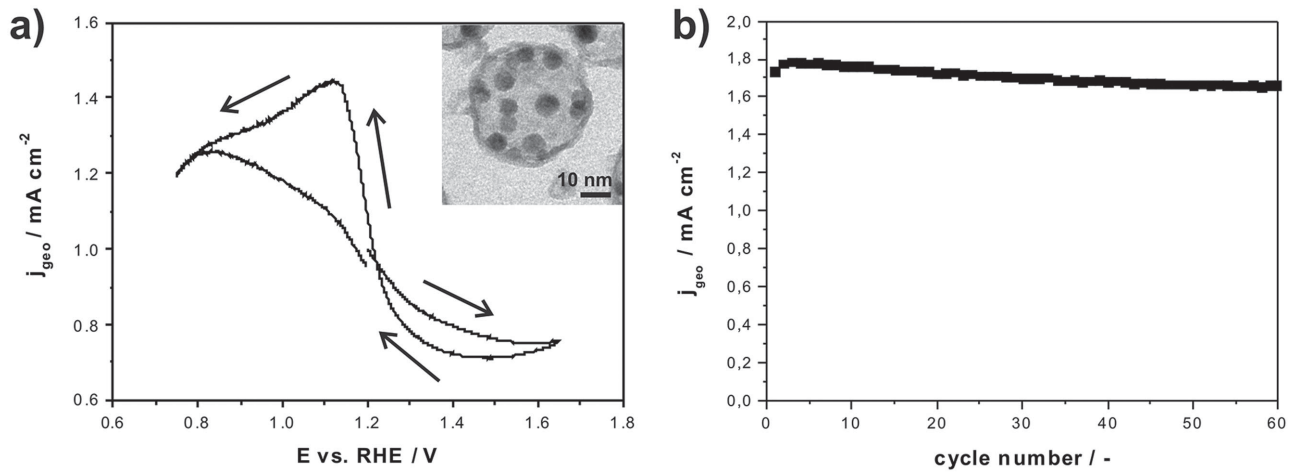

Figure 8. a) Cyclic voltammogram of $Au0.6_{NP}@ITO_{TR}$ (black line) measured in a CO saturated 0.1 M NaOH electrolyte (fifth scan, 5 mV s^{-1}, 1600 rpm). The current is normalized to the geometric area of the electrode. b) CO oxidation current density maxima, determined in each cycle, plotted against the cycle number (time).

electrocatalytic CO oxidation in alkaline media. In this context, CO oxidation was chosen as it represents the model reaction in terms of gold based catalysis[36,37] and electrocatalysis.[24,38,39] For that purpose an $Au0.6_{NP}@ITO_{TR}$ yolk@shell thin film was coated on a glassy carbon electrode and subjected to cyclic voltammetry (CV) between 0.75 and 1.65 V_{RHE} in a nitrogen degassed electrolyte to clean the gold surface. Subsequently, the electrolyte was saturated with CO and the CO oxidation activity was determined by CV in the same potential interval (for details see the Experimental Section). In line with other Au_{NP}–ITO electrodes,[24,38,39] the $Au0.6_{NP}@ITO_{TR}$ hollow spheres show a pronounced CO oxidation activity, as demonstrated by the pronounced CO oxidation current with a current maximum of 1.5 mA cm^{-2} (geometric surface area) at around 1.1 V_{RHE} (**Figure 8**a, red curve, scanning speed = 5 mV s^{-1}, fifth cycle). As such, we can conclude that the gold nanoparticles inside the ITO_{TR} hollow spheres are accessible to the CO saturated electrolyte and highly active for CO oxidation. The stability during CO oxidation was also probed by CV, though with faster scan rate (100 mV s^{-1}). The current density maximum of each cycle was plotted against the cycle number as measure of the stability. When compared to non-yolk@shell Au_{NP}–ITO nanocomposites,[24,38,39] the CO oxidation current density is quite stable and decreases only slightly over repeated cycling. Indeed, while for other Au_{NP}–ITO structures a drastic decay of the CO oxidation current density is observed (the current density drops at least by 70%),[24,38,39] the CO oxidation current density of $Au_{NP}@ITO_{TR}$ only decreases by ≈4% over 60 cycles.

2.9. $Au_{NP}@ITO_{TR}$ Yolk@Shell Thin Films: From Spherical to Worm-Like Structures

Finally, as a final challenge and to demonstrate the versatility of our approach, we synthesized nonspherical yolk@shell materials.[40–42] By simply varying the block length of the PS-*b*-P4VP template (Table 1),[43,44] block copolymer micelles with worm-like structure could be assembled in solution (see TEM data (**Figure 9**a)) and SAXS data analysis in Figure S21 (Supporting

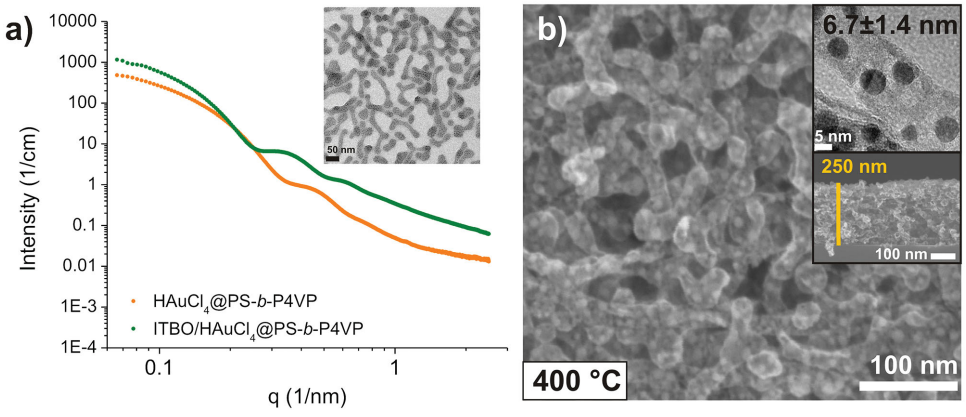

Figure 9. a) SAXS measurements of worm-like $HAuCl_4 \cdot 3H_2O$ (0.6 eq.) loaded PS-*b*-P4VP micelles in toluene before (orange) and after the addition of ITBO (green). Inset: TEM image of worm-like $HAuCl_4$ loaded PS-*b*-P4VP micelles. b) SEM of $Au_{NP}@ITO_{TR}$ yolk–shell based thin film with worm-like structure. Inset: Corresponding TEM image and SEM cross section.

Information). Similar to their spherical counterparts these worm-like micelles, once loaded with $HAuCl_4 \cdot 3H_2O$, could easily be used as nanoreactor templates for the synthesis of Au_{NP}@ITO_{TR} yolk@shell thin films. In line with the micellar shape and dimensions, Au_{NP}@ITO_{TR} yolk@shell structures with a worm-like morphology are formed, with a diameter of ≈25 nm and a length of several 100 nm (see Figure S21, Supporting Information). As for their spherical counterparts, these worm-like structures are homogeneously loaded with uniformly sized Au_{NP}, which again reveal a diameter of ≈6 nm (Figure 9b).

3. Conclusion

In this contribution, a supramolecular approach allowing the one-pot synthesis of Au_{NP}@ITO_{TR} yolk@shell nanostructures is presented. Our approach, entitled hydrophobic nanoreactor templating, relies on PS-*b*-P4VP inverse micelles as two-compartment nanoreactor templates. While the hydrophilic micellar core serves as reservoir for the hydrophilic and acidic gold precursor ($HAuCl_4 \cdot 3H_2O$), the hydrophobic PS shell allows the incorporation of the hydrophobic ITO_{TR} precursor (indium(I)tin(II)tri-*tert*-butoxide). As a result, hybrid core–shell precursor micelles are obtained, which enable the formation of various Au_{NP}/ITO_{TR} nanostructures after solvent evaporation and calcination. The final Au_{NP}/ITO_{TR} nanostructure depends on the precursor's stoichiometry within the micelles. While for low metal loadings, Au_{NP}/ITO_{TR} nanostructures with an open porous structure and one metal nanoparticle per pore are obtained, higher metal loadings lead to the formation of Au_{NP}@ITO_{TR} yolk@shell nanostructures containing several evenly sized and fully accessible Au nanoparticles. Taking advantage of the conductivity and porosity of the ITO_{TR} shell, the as-synthesized AuNP@ITO_{TR} yolk@shell structures feature high and durable activity for CO electrooxidation. Considering that these highly complex metal@metal oxide yolk@shell structures are simply obtained by mixing three components in solution, i.e., a metal affine amphiphilic block copolymer; a hydrophilic, hydrated, and acidic metal precursor; and a hydrophobic alkoxodic hydrolysis prone oxide precursor—our approach offers an easy and scalable synthetic pathway for metal@metal oxide yolk@shell nanomaterials with potential applications in catalysis and other energy-related applications.

4. Experimental Section

Materials: Tetrachloroauric (III) acid ($HAuCl_4 \cdot 3H_2O$, Roth) was used as received and stored in a dry glove box (<1 ppm H_2O, <1 ppm O_2). Polystyrene-*block*-poly(4-vinylpyridine), PS_{111}-*b*-$P4VP_{96}$ and PS_{135}-*b*-$P4VP_{137}$ were synthesized in the group of Prof. Helmut Schlaad as reported in literature by sequential anionic polymerization of styrene and 4-vinylpyridine (initiator: *sec*-butyllithium/LiCl, solvent: THF, –78 °C).[43,45,46] The molar ratios S:4VP were determined by ^{1}H-NMR ($CDCl_3$) and the number- and weight-average molar masses were determined by size exclusion chromatography (THF, PS calibration) and are listed in Table 1.

Synthesis of ITBO: The heterobimetallic single source precursor ITBO was synthesized as previously reported.[21,22] Briefly, to a suspension of InBr in anhydrous toluene a concentrated solution of $Na(OtBu)_3Sn$ in toluene was added under vigorous stirring. The reaction mixture was refluxed at 110 °C for 48 h. After cooling to room temperature, insoluble by-products were removed by filtration. The solvent of the filtrated solution was removed under vacuum and the obtained white product was recrystallized in pentane and stored at –24 °C. The obtained precursor was characterized by ^{1}H-NMR (C_6D_6, 200.13 MHz, δ = 1.36 ppm [1s, 27 H, $OC(C\underline{H}_3)_3$]) and ^{119}Sn-NMR spectroscopy (C_6D_6,149.21 MHz, δ = –78 ppm).

Table 2. Mass of $HAuCl_4 \cdot 3H_2O$ to be added to 1 mL of 30 mg mL^{-1} PS_{111}-*b*-$P4VP_{96}$ micellar solution.

$HAuCl_4 \cdot 3H_2O$ eq. per pyridine unit	0.3	0.6
$HAuCl_4 \cdot 3H_2O$ mass [mg] to be added to 1 mL of 30 mg mL^{-1} PS_{111}-*b*-$P4VP_{96}$ solution	14.4	28.8
$HAuCl_4 \cdot 3H_2O$ mass [mg] to be added to 1 mL of 30 mg mL^{-1} PS_{135}-*b*-$P4VP_{137}$ solution	–	36.0

Synthesis of Mesoporous ITO_{TR} Thin Films with One Au_{NP} Per Pore: For the preparation of mesoporous ITO_{TR} thin films loaded with one AuNP per pore, a stock solution of PS-*b*-P4VP with a concentration of 5 mg mL^{-1} was prepared by dissolving the corresponding amount of PS-*b*-P4VP in anhydrous toluene. After 20 min of stirring, 1 mL of this solution was added to 1.6 mg of $HAuCl_4 \cdot 3H_2O$ (0.2 eq. $HAuCl_4 \cdot 3H_2O$ per pyridine unit, $HAuCl_4$(0.2)@PS-*b*-P4VP). The resulting solution was stirred for 12 h to ensure a homogeneous loading. After that, 1 mL of this solution was added to 25 mg of solid ITBO so that $n(HAuCl_4)/n(ITBO)$ = 0.07. The solution was spin-coated (spinning speed between 3000 and 6000 rpm) on selected substrates (Si wafers, glass, or ITO-coated glass substrates). The obtained films were dried for 1 h inside the glovebox prior to calcination in air at 400 °C for 2 h (heating rate: 5 °C min^{-1}) and in reducing atmosphere (10% H_2, 90% N_2, 300 °C, 90 min).

Synthesis of AuX_{NP}@ITO_{TR} Yolk@Shell Based Thin Films: For the preparation of $HAuCl_4(X)$@PS_m-*b*-$P4VP_n$ solutions, first a stock solution of PS_m-*b*-$P4VP_n$ (30 mg mL^{-1}) was prepared in anhydrous toluene. For a gold precursor loading of *X* eq. per pyridine unit, 1 mL of the previous PS_m-*b*-$P4VP_n$ stock solution was added to the appropriate amount of $HAuCl_4 \cdot 3H_2O$ (see **Table 2**). After addition, the resulting solution ($HAuCl_4(X)$@PS_m-*b*-$P4VP_n$) was stirred for 12 h to ensure a homogeneous loading of the metal precursor throughout the micellar solution. Note: The $HAuCl_4(X)$@PS_m-*b*-$P4VP_n$ solutions have to be used in less than 48 h to obtain reproducible results. For the preparation of $Au(X)_{NP}$@ITO_{TR} thin films, 1 mL of the respective $HAuCl_4(X)$@PS_m-*b*-$P4VP_n$ was added to 60 mg of ITBO (ITBO/Au(*X*)@PS_{111}-*b*-$P4VP_{96}$). Prior addition, ITBO, which is stored at –20 °C, is warmed to room temperature. After addition, the ITBO/$HAuCl_4(X)$@PS_m-*b*-$P4VP_n$ mixture was stirred for 10 min at room temperature. The resulting brown viscous ITBO/$HAuCl_4(X)$@PS_m-*b*-$P4VP_n$ solution was then spin-coated on selected substrates (spinning speed: between 3000 and 6000 rpm, substrates: Si wafers, glass, or ITO-coated glass substrates (Aldrich)). The obtained films, once dried, were then directly calcined under air for 2 h (heating ramp 5°C min^{-1}). Finally, in order to increase the conductivity, the films were calcined under reducing atmosphere (in 10% H_2, 90% N_2, 300 °C, 90 min).

Synthesis of Au0.6$_{NP}$@ITO_{TR} Yolk@Shell Based Bilayers: For the preparation of Au0.6$_{NP}$@ITO_{TR} yolk@shell based bilayers, the same procedure was applied. The concentration of polymer was adjusted to 10 mg mL^{-1} instead of 30 mg mL^{-1}. The amount of gold was consequently adjusted (see **Table 3**).

Characterization Methods: NMR spectroscopy was performed on an ARX 200 (^{1}H 200 MHz) and an ARX 400 (^{1}H 400 MHz, ^{119}Sn

Table 3. Mass of $HAuCl_4 \cdot 3H_2O$ to be added to 1 mL of PS_{111}-*b*-$P4VP_{96}$ micellar solution with a concentration of 10 mg mL^{-1}.

$HAuCl_4 \cdot 3H_2O$ eq. per pyridine unit	0.3	0.6
$HAuCl_4 \cdot 3H_2O$ mass [mg] to be added to 1 mL of 5 mg mL^{-1} PS_{111}-*b*-$P4VP_{96}$ solution	4.8	9.6

149.21 MHz) spectrometer from Bruker. UV–vis spectroscopy was performed in transmission on a Perkin-Lambda 20 spectrometer under inert atmosphere using a quartz glass cuvette as sample holder.

Time-dependent Maxwell equations were solved by numerical finite difference time domain (FDTD) simulations. Au/ITO yolk@shell structures were assumed to be illuminated by polarized light in the spectral range between 400 and 800 nm. The 3D geometry consisted of ITO spheres of radius $r = 20$ nm containing six Au spheres of radius $r = 3$ nm each. The index of refraction of ITO was set to $n = 1.93$ in the considered spectral range. Corresponding data for Au were taken from the CRC Handbook of Chemistry and Physics.

XRD was performed either with a Bruker-AXS D8 Advanced diffractometer with a DAVINCI design using CuKα radiation ($\lambda = 1.5418$ Å) and a LynxEye detector or at the high energy material science (HEMS) P07 side station beamline of the DORIS III synchrotron source at the DESY facility (Hamburg, Germany). The synchrotron measurements were made with a sample-to-detector distance of 930.8 mm, at a photon energy of 53.7 keV (i.e., $\lambda \approx 2.3088$ Å), and with a single-photon counting pixel detector MAR345 (image plate).

Krypton sorption isotherms were measured at 77 K using a Quantachrome Instrument ASI-C-11. The film samples were degassed under vacuum at 150 °C for 6h prior measurement. The surface area was calculated using the Brunauer–Emmett–Teller (BET) method.

SAXS was conducted at the B1 beamline of the DORIS III synchrotron source and at the P03 beamline at PETRA III at synchrotron at DESY (Hamburg, Germany). The data were normalized to absolute intensity scale using a glassy carbon reference. At the B1 beamline of the DORIS III synchrotron source, measurements were made with a sample-to-detector distance of 3.6 m, at a photon energy of 11.5 keV ($\lambda \approx 1.08$ Å), and with a single-photon counting pixel detector Pilatus 1M (Dectris). At the P03 beamline at PETRA III at the synchrotron at DESY, measurements were made with a sample-to-detector distance of 3.95 m, at a photon energy of 13 keV ($\lambda \approx 0.957$ Å), and with a Pilatus 300k (Dectris) pixel detector. The collected 2D images were azimuthally integrated to 1D curves, corrected for sample transmission and background scattering. The quartz capillaries used for solution measurements were filled and sealed in a glove box and stored on dry ice prior measurements. The polymer concentration was kept constant (5 mg mL^{-1}).

ASAXS was conducted at the B1 beamline of the DORIS III synchrotron source. The ASAXS curves were recorded at three different energies in close vicinity of the Au L_3 absorption edge (^{79}Au L_3, E_{Au} = 11 919 eV, E_1 = 11 527 eV, E_2 = 11 873 eV, and E_3 = 11 915 eV). The sample-to-detector distance was 3.6 m and the total measurement time was about 120 s for each sample. Briefly, the scattering length density ρ of an atom depends on the atomic scattering factor $f(E)$, which at low scattering angles can be expressed by

$$f(E) = Z + f'(E) + if''(E) \tag{3}$$

where E is the energy, Z the atomic number, and f' and f'' anomalous scattering coefficients, which change rapidly close to an absorption edge of an element. More details can be found in the Supporting Information.

Evaluation of the SAXS Data: Data evaluation was done using SASFit.[47] In the case of spherical micelles (PS_{111}-*b*-$P4VP_{96}$), the SAXS curves were analyzed with a spherical core–shell model, assuming a spherical shape of the micelles, a core–shell distribution of the electron density, and a Schultz–Zimm size distribution (D_{SZ}). The respective form factor F_{CS}, i.e., spherical shell (iii), was used as defined in the SASFit package[47] (see details in the Supporting Information).

In the case of worm-like micelles (PS_{135}-*b*-$P4VP_{137}$) no data fitting was performed. Instead, a Guinier analysis was performed. The radius of gyration of the transversal cross section, R_C, was determined from the intermediate-q Guinier approximation[48]

$$I(q) = \frac{I(0)}{q} \exp\left(-\frac{q^2 R_C^2}{2}\right) \tag{4}$$

R_C was determined from the slope of the Guinier plot in which $\ln(q \times I(q))$ is plotted versus q^2.

X-Ray Absorption Near Edge Spectroscopy (XANES): XAS Sample Preparation: Solid reference In(III)(O*t*Bu)$_3$ and Sn(II)(O*t*Bu)$_2$ powders were diluted with boron nitride (Sigma Aldrich Chemie GmbH Munich, GER) in a mass ratio of 1:10. A custom-made mount made of a 3 mm thick polyoxomethylene (POM) sheet with a 0.5 × 1.5 cm^2 window through which the samples are accessible for the X-rays was specially designed as sample holder. To contain the samples, the window was sealed from both sides with a single layer of Kapton foil (0.013 mm, Goodfellow GmbH, Bad Nauheim, GER) using a one-component adhesive sealant (Sinus Electronic TSE399C, Bad Wimpfen, GER) for fixation. ITBO solutions were prepared in toluene at a concentration of 10×10^{-3} M. For measurements 200 µL of each solution was injected in the volume defined by the two Kapton sealed windows of the sample holder. Once sealed the sample was removed from the glove box and promptly frozen in liquid nitrogen in which it was stored until the measurements.

XAS Measurements: The XAS measurements at the indium and tin L-edges were performed at the KMC-1 bending magnet beamline of the Helmholtz-Zentrum Berlin for Materials and Energy (formerly BESSY II, Berlin). The beamline optics and beam characteristics are discussed elsewhere.[49] The specifications of the used setup developed by the group of Prof. H. Dau are already well described.[50,51] The excitation energies (scan range 3623–4530 eV for indium and tin) were selected by a double-crystal monochromator (Si-111). An energy-resolving fluorescence detector with 13 Ge elements (Ultra-LEGe detectors, Canberra GmbH) was employed. Indium and tin edges were recorded simultaneously (Lβ_3 and Lβ_1 emission of tin, Lα_1 emission of indium). Details about data extraction are provided in Figure S14 (Supporting Information).

XPS measurements were carried out using an ultrahigh vacuum system from SPECS, Germany. Photoelectrons were excited by an MgKα X-ray source of 1253.6 eV excitation energy.

TEM and EDX measurements were performed on a TECNAI G^{2}20 S-TWIN electron microscope operated at 200 kV, equipped with an EDAX EDX system (Si(Li) SUTW detector, energy resolution of 136 eV (for MnKα)). For sample preparation, a drop of diluted solution was deposited onto selected TEM grids (i.e., carbon-coated copper grids or thermally stable silicon nitride membrane grids for calcination studies). After solution adsorption on the grid surface, the excess of solution was removed from the grid with a filter paper, leaving behind a micellar monolayer. For TEM investigations of the nanoparticle growth, the silicon nitride grids were calcined at different temperatures. For investigations of the films after calcination, bits of the films were scraped off the substrate and transferred onto a carbon-coated copper grid.

SEM was performed using a JEOL 7401F electron microscope equipped with an in-lens secondary electron detector. Image J Version 1.39u (http://rsbweb.nih.gov/ij/) was employed to determine the yolk–shell particle diameters, the Au^0 NP size distribution, and the FFTs of the SEM and TEM images.

Conductivity measurements were performed by four-point probe measurements at room temperature with a resistivity meter Loresta-GP model MCP-T610, PSP 1.5 mm from Mitsubishi Chemical Analytech. The specific resistivity (Ω cm) of the films was calculated by multiplying the sheet resistance (Ω $^{-1}$) by the film thickness. Undoped Si wafers (225 µm, (100), 20 000 Ω cm) were chosen as nonconductive substrates. For the conductivity measurements, the yolk–shell based thin films were deposited onto nonconductive Si wafers, previously coated with an ultra thin tin-rich ITO layer (10 nm) to improve the adhesion and ensure lateral conductivity.

Electrochemical measurements were performed with a rotating disk electrode (RDE) setup in a three-compartment electrochemical glass cell equipped with a Luggin capillary and glass frit separating the working and counter electrode compartments. A reversible hydrogen electrode (RHE) (Gaskatel), immersed in the same electrolyte, served as reference and a platinum mesh as counter electrode. The 0.1 M NaOH electrolyte was prepared from sodium hydroxide (Sigma-Aldrich, 99.99%) and

ultrapure water (18 MΩ cm at room temperature). The potential was controlled with an SP-200 potentiostat (BioLogic). For the experiments, the $Au(0.6)_{NP}@ITO_{TR}$ yolk@shell thin film (a bilayer) was coated on the abutting face of a previously polished and cleaned glassy carbon cylinder (5 mm diameter), which was then mounted into an RDE tip (Teflon) (Pine Research Instrumentation) and connected to the RDE setup described above. The electrode was cycled in the N_2 saturated electrolyte between 0.75 and 1.65 V_{RHE} (30 cycles). Subsequently, the electrolyte was bubbled with CO (15 min) while the electrode potential was set to 1.2 V_{RHE}. Thereafter, CV was measured with 5 mV s^{-1} between 0.75 and 1.65 V_{RHE} (five cycles) to address the CO oxidation activity. To address the catalyst stability CVs were measured, after a second CO bubbling step, with 100 mV s^{-1} in the same potential range as before for 60 cycles. During the CO oxidation measurements CO was flowing above the electrolyte and the RDE rotational speed was adjusted to 1600 rpm. The initial cycling in N_2 saturated electrolyte was conducted without rotation.

Supporting Information

Supporting Information is available from the Wiley Online Library or from the author.

Acknowledgements

Financial support from the Cluster of Excellence "Unifying Concepts in Catalysis" EXC-314/2 (supported by the Deutsche Forschungsgemeinschaft and administered by the Technical University Berlin) is gratefully acknowledged. In addition, A.F. thanks the BMBF for generous funding of the project EDELKAT (FZ 03X5524) as well as the DFG for financial support with the project FI 1885/1-1. T.R. and P.S. acknowledge financial support by the DFG under the Priority Program 1613 "Fuels Produced Regeneratively through Light-Driven Water Splitting." BESSY, DESY, and the Helmholtz-Zentrum Gesellschaft are gratefully acknowledged for allocation of beamtime.

Received: June 11, 2015
Revised: July 14, 2015
Published online: September 11, 2015

[1] S. Wang, M. Zhang, W. Zhang, *ACS Catal.* **2011**, *1*, 207.
[2] J. Lee, J. C. Park, H. Song, *Adv. Mater.* **2008**, *20*, 1523.
[3] C. Galeano, R. Güttel, M. Paul, P. Arnal, A.-H. Lu, F. Schüth, *Chem. Eur. J.* **2011**, *17*, 8434.
[4] G. Li, Z. Tang, *Nanoscale* **2014**, *6*, 3995.
[5] J. Liu, S. Z. Qiao, J. S. Chen, X. W. D. Lou, X. Xing, G. Q. M. Lu, *Chem. Commun.* **2011**, *47*, 12578.
[6] X. Fang, Z. Liu, M.-F. Hsieh, M. Chen, P. Liu, C. Chen, N. Zheng, *ACS Nano* **2012**, *6*, 4434.
[7] J.-W. Yoon, Y. J. Hong, Y. C. Kang, J.-H. Lee, *RSC Adv.* **2014**, *4*, 16067.
[8] L. Wang, H. Dou, Z. Lou, T. Zhang, *Nanoscale* **2013**, *5*, 2686.
[9] W.-M. Zhang, J.-S. Hu, Y.-G. Guo, S.-F. Zheng, L.-S. Zhong, W.-G. Song, L.-J. Wan, *Adv. Mater.* **2008**, *20*, 1160.
[10] Y. J. Hong, M. Y. Son, Y. C. Kang, *Adv. Mater.* **2013**, *25*, 2279.
[11] B. Liu, J. Wang, S. Sun, X. Wang, M. Zhao, W. Zhang, H. Zhang, X. Yang, *RSC Adv.* **2013**, *3*, 18506.
[12] G. Wang, J. Hilgert, F. H. Richter, F. Wang, H. Bongard, B. Spliethoff, C. Weidenthaler, F. Schüth, *Nat. Mater.* **2014**, *13*, 293.
[13] C. Galeano, C. Baldizzone, H. Bongard, B. Spliethoff, C. Weidenthaler, J. C. Meier, K. J. J. Mayrhofer, F. Schüth, *Adv. Funct. Mater.* **2014**, *24*, 220.
[14] R. Liu, F. Qu, Y. Guo, N. Yao, R. D. Priestley, *Chem. Commun.* **2014**, *50*, 478.
[15] J. C. Park, H. Song, *Nano Res.* **2010**, *4*, 33.
[16] M. Paul, F. Schu, R. Gu,*Catal. Sci. Technol.* **2011**, *1* , 65.
[17] P. M. Arnal, M. Comotti, F. Schüth, *Angew. Chem., Int. Ed.* **2006**, *45*, 8224.
[18] X. Huang, C. Guo, J. Zuo, N. Zheng, D. Stucky, *Small* **2009**, *5*, 361.
[19] C. Galeano, C. Baldizzone, H. Bongard, B. Spliethoff, C. Weidenthaler, J. C. Meier, K. J. J. Mayrhofer, F. Schüth, *Adv. Funct. Mater.* **2013**, *24*, 220.
[20] J. Liu, S. Z. Qiao, J. S. Chen, X. W. Lou, X. Xing, G. Q. Lu, *Chem. Commun.* **2011**, *47*, 12578.
[21] Y. Aksu, M. Driess, *Angew. Chem., Int. Ed. Engl.* **2009**, *48*, 7778.
[22] M. Veith, K. Kunze, *Angew. Chem., Int. Ed. Engl.* **1991**, *30*, 95.
[23] Y. Aksu, S. Frasca, U. Wollenberger, M. Driess, A. Thomas, *Chem. Mater.* **2011**, *23*, 1798.
[24] A. Guiet, T. Reier, N. Heidary, D. Felkel, B. Johnson, U. Vainio, H. Schlaad, Y. Aksu, M. Driess, P. Strasser, A. Thomas, J. Polte, A. Fischer, *Chem. Mater.* **2013**, *25*, 4645.
[25] J. Chen, M. Arafeh, A. Guiet, D. Felkel, A. Loebus, S. M. Kelleher, A. Fischer, M. C. Lensen, *J. Mater. Chem. C* **2013**, *1*, 7709.
[26] M. S. M. Antonietti, E. Wenz, L. Bronstein, *Adv. Mater.* **1995**, *7*, 1000.
[27] G. Kästle, H.-G. Boyen, F. Weigl, G. Lengl, T. Herzog, P. Ziemann, S. Riethmüller, O. Mayer, C. Hartmann, J. P. Spatz, M. Möller, M. Ozawa, F. Banhart, M. G. Garnier, P. Oelhafen, *Adv. Funct. Mater.* **2003**, *13*, 853.
[28] J. P. Spatz, S. Modmer, M. Moiler, *Chem. Eur. J.* **1996**, *2*, 1552.
[29] A. Guiet, T. Reier, N. Heidary, D. Felkel, B. Johnson, U. Vainio, H. Schlaad, Y. Aksu, M. Driess, P. Strasser, A. Thomas, J. Polte, A. Fischer, *Chem. Mater.* **2013**, *25*, 4645.
[30] K. Samedov, Y. Aksu, M. Driess, *Chem. Eur. J.* **2012**, *18*, 7766.
[31] J. Beckmann, K. Jurkschat, S. Rabe, M. Schu, *Zeitschrift für Anorg. und Allg. Chemie* **2001**, *627*, 458.
[32] M. A. Aouaj, R. Diaz, A. Belayachi, F. Rueda, M. Abd-Lefdil, *Mater. Res. Bull.* **2009**, *44*, 1458.
[33] M. S. Hwang, B. Y. Jeong, J. Moon, S. K. Chun, J. Kim, *Mater. Sci. Eng., B* **2011**, *176*, 1128.
[34] G. Mie, *Ann. Phys.* **1908**, *25*, 377.
[35] F. Goettmann, A. Moores, C. Boissière, P. Le Floch, C. Sanchez, *Small* **2005**, *1*, 636.
[36] M. Haruta, *Chem. Rec.* **2003**, *3*, 75.
[37] M. Haruta, *Catal. Today* **1997**, *36*, 153.
[38] B. R. Cuenya, S.-H. Baeck, T. F. Jaramillo, E. W. McFarland, *J. Am. Chem. Soc.* **2003**, *125*, 12928.
[39] T. F. Jaramillo, S.-H. Baeck, B. R. Cuenya, E. W. McFarland, *J. Am. Chem. Soc.* **2003**, *125*, 7148.
[40] X. W. Lou, C. Yuan, L. A. Archer, *Adv. Mater.* **2007**, *19*, 3328.
[41] B. Xiong, W. David, L. A. Archer, *Adv. Mater.* **2008**, *20*, 3987.
[42] J. Liu, S. Z. Qiao, S. B. Hartono, G. Q. M. Lu, *Angew. Chem., Int. Ed. Engl.* **2010**, *49*, 4981.
[43] M. Antonietti, S. Heinz, M. Schmidt, C. Rosenauer, *Macromolecules* **1994**, *27*, 3276.
[44] F. Calderara, G. Riess, E. Nationale, S. De Chimie, A. Werner, *Macromol.Chem. Phys.* **1996**, *197*, 2115.
[45] S. Schrage, R. Sigel, H. Schlaad, **2003**, *36*, 1417, *Macromolecules*.
[46] F. Boss, H. P. Schreiberf, A. Eisenberg, *Macromolecules* **1993**, *26*, 6447.
[47] http://sasfit.ingobressler.net.(accessed: April 2015)
[48] O. Glatter, O. Kratky, *Small Angle X-Ray Scattering*, Academic Press, London, UK **1982**.
[49] F. Schaefers, M. Mertin, M. Gorgoi, *Rev. Sci. Instrum.* **2007**, *78*, 123102.
[50] M. Risch, K. Klingan, F. Ringleb, P. Chernev, I. Zaharieva, A. Fischer, H. Dau, *ChemSusChem* **2012**, *5*, 542.
[51] M. Risch, K. Klingan, J. Heidkamp, D. Ehrenberg, P. Chernev, I. Zaharieva, H. Dau, *Chem. Commun.* **2011**, *47*, 11912.